# The Effect of the Charge Transfer Transition of the Tetravalent Terbium on the Photostability of Oxide Thin-Film Transistors

*Linfeng Lan,\* Xiao Li, Chunchun Ding, Siting Chen, Huimin Su, Bo Huang, Baozhong Chen, Hongkun Zhou, and Junbiao Peng\**

The development of the next-generation display technologies requires thin-film transistors (TFTs) with high mobility and good negative-bias-illumination stress (NBIS) stability. Here, a tetravalent-terbium-doped indium oxide ($Tb:In_2O_3$) semiconductor is reported, which can effectively improve the NBIS stability of the TFT while ensuring high mobility. The TFT with $Tb:In_2O_3$ channel layer exhibited remarkable performance with a saturation mobility of 45.0 $cm^2$ $V^{-1}$ $s^{-1}$ (with average mobility of 38.6 $cm^2$ $V^{-1}$ $s^{-1}$), a turn-on voltage ($V_{on}$) of −1.1 V, and an on-off current ratio of $10^8$. In addition, the $Tb:In_2O_3$ TFT showed greatly improved NBIS stability with $V_{on}$ shift ($\Delta V_{on}$) of −3.9 V (with average $\Delta V_{on}$ of 4.0 V) under 3600 s stress with −20 V gate voltage and white light illumination (compared to $\Delta V_{on}$ of −11.7 V for the pure $In_2O_3$ TFT). Comprehensive studies reveal that the effective improvement of NBIS stability after $Tb^{4+}$ doping is mainly attributed to the wide-band absorption of the incident blue light by the $Tb4f\,^7$—$O2p^6$ to $Tb4f\,^8$—$O2p^5$ charge transfer (CT) transition that has smaller overall lattice expansion/contraction and shorter relaxation time compared to $V_O$ ionization.

## 1. Introduction

Since Hosono et al. demonstrated the first amorphous $InGaZnO_4$ (a-IGZO) thin-film transistors (TFTs) in 2004,[1] amorphous oxide semiconductors (AOSs) have drawn considerable attention owing to their relatively high mobility, low-temperature and large-area processability, good uniformity, and high transparency. Especially, the extremely low off current ($I_{off}$) makes it become the best candidate for the channel materials of the addressing TFTs for energy-saving displays. For example, the power consumption of the smart bracelets (watches) can be reduced effectively when using low-temperature polycrystalline oxide instead of low-temperature polysilicon (LTPS) as the TFT backplanes.[2]

However, the AOS TFTs suffer from serious threshold voltage change under negative-bias-illumination stress (NBIS), which may be attributed to the ultra-long relaxation time of the photo-induced oxygen vacancy ($V_O$) ionization.[3–8] Recent work shows that widening bandgap of the AOSs can enhance the stability under NBIS, but the mobility decreases seriously because it requires high Ga concentration (70 at.%).[9] The results reveal that there is a tradeoff between the mobility and the NBIS stability of the AOS TFTs.[10] Although the mobility of the AOS TFTs with good NBIS stability is generally greater than that of the amorphous silicon (a-Si), it is still much lower than some practical requirements of the next generation of display technologies, such as super-high-vision technologies based on organic light-emitting diodes (LEDs) or micro-LEDs, which generally require TFTs with a mobility higher than 40 $cm^2$ $V^{-1}$ $s^{-1}$.[10] Therefore, designing new AOS materials with mobility closed to or higher than that of LTPS as well as with good NBIS stability is attractive in new display technologies.

Our previous work shows that praseodymium (Pr) and terbium (Tb) can improve the NBIS stability of the AOS TFTs greatly, because the charge transfer (CT) transition of the $Pr^{4+}$ or $Tb^{4+}$ can absorb the whole range of blue light and downconverting into nonradiative transition.[11] However, the mobility is still less than 15 $cm^2$ $V^{-1}$ $s^{-1}$, which may be owing to the relatively poor film quality and high impurity density resulting from the residue impurities during solution process. In this letter, terbium-doped indium oxide ($Tb:In_2O_3$) AOS TFTs were fabricated by vacuum process (sputtering) to find out the upper mobility limit of the new materials while keeping good NBIS stability. Meanwhile, new experiments and analyses are carried out to give a more insightful understanding of the mechanism of the NBIS stability improvement after $Tb^{4+}$ doping. It is worth noting that Tb (rather than Pr) was employed because it has smaller ion radius compared to Pr due to the lanthanide contradiction, which is closer to that of $In^{3+}$. It means that incorporating Tb into $In_2O_3$ has less lattice distortion, which may result in higher mobility compared to Pr doped $In_2O_3$.

L. Lan, X. Li, C. Ding, S. Chen, H. Su, B. Huang, B. Chen, H. Zhou, J. Peng
State Key Laboratory of Luminescent Materials and Devices
South China University of Technology
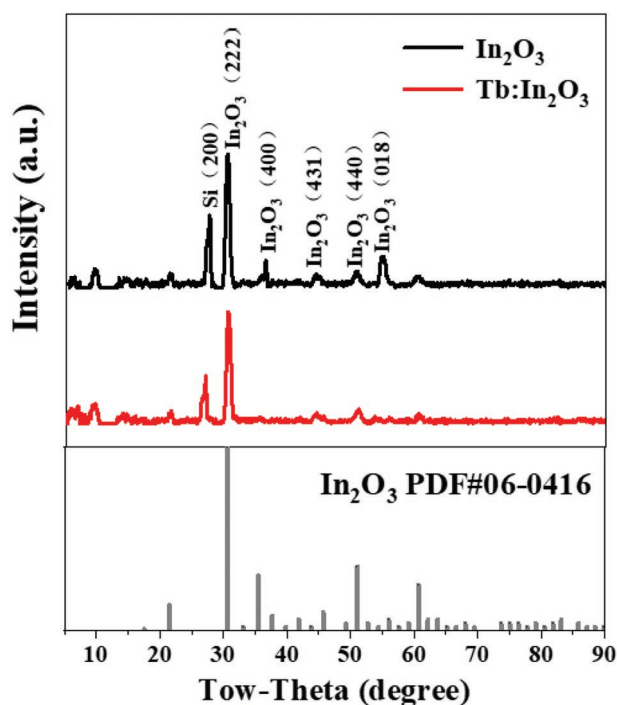Guangzhou 510640, China
E-mail: lanlinfeng@scut.edu.cn; psjbpeng@scut.edu.cn

**Figure 1.** XRD patterns of the $In_2O_3$ and $Tb:In_2O_3$ films, and the bottom pattern is the standard refraction pattern of the single-crystal bixbyite $In_2O_3$.



**Figure 2.** a) Schematic structure of the TFTs; the transfer characteristics and $I_G$ versus $V_G$ curves of the b) $In_2O_3$ and c) $Tb:In_2O_3$ TFTs; d) saturation mobility versus $V_G$ plot of the $Tb:In_2O_3$ TFT; e) the mobility distribution histogram of the 125 $Tb:In_2O_3$ TFTs fabricated with the same condition.

## 2. Results and Discussion

The structure of the sputtered $In_2O_3$ and $Tb:In_2O_3$ ($Tb_4O_7$/$In_2O_3$=5/95 wt.) films were investigated using X-ray diffraction (XRD), as shown in **Figure 1**. The pure $In_2O_3$ film without Tb doping exhibited clear nanocrystalline nature with $In_2O_3$ bixbyite structure, which is consistent with the standard value for bulk cubic-$In_2O_3$.[12] The grain size of the pure $In_2O_3$ film was calculated by Scherrer equation to be ≈10.8 nm, no much difference compared to that of the $Tb:In_2O_3$ film (≈10.7 nm). Meanwhile, it was observed that the (222) peaks of $In_2O_3$ and $Tb:In_2O_3$ were at the same position (30.54°), indicating little lattice expansion after doping with $Tb_4O_7$. Figure S1a, Supporting Information, shows the scanning transmission electron microscopy (STEM) image and the corresponding elements distribution maps obtained from energy-dispersion X-ray spectroscopy (EDS) for the sample with Glass/Al:Nd/Nd:AlO$_x$ (200 nm)/$Tb:In_2O_3$ (80 nm) structure. The distribution of the Tb fluctuated slightly in the film. The depth profiles of the Tb and In atoms in the $Tb:In_2O_3$ film were characterized by time-of-flight secondary-ion mass spectrometry (TOF-SIMS), as shown in Figure S1b, Supporting Information. The Tb atoms existed in the whole $Tb:In_2O_3$ film, but the distribution fluctuated slightly with the average atomic Tb to (Tb+In) ratio of ≈4.2 at.%. The microstructure of the $Tb:In_2O_3$ film was further examined by using high-resolution transmission electron microscopy (HR-TEM) and fast Fourier transform (FFT) analysis, as shown in Figure S1c, Supporting Information. It revealed a polycrystalline structure of $Tb:In_2O_3$ with different crystal plane orientations.

TFTs with different channels were fabricated with the bottom-gate, top-contact structure, as shown in **Figure 2a**. The transfer curves of the $In_2O_3$ and $Tb:In_2O_3$ TFTs are shown in
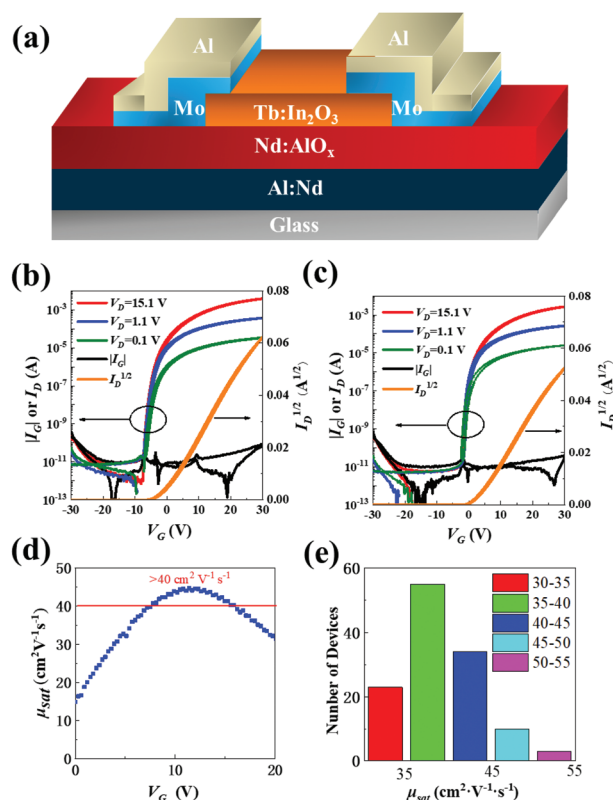
Figure 2b,c, respectively. And the corresponding output curves of the $In_2O_3$ and $Tb:In_2O_3$ TFTs are shown in Figure S2b,c, Supporting Information, respectively. The saturation mobility ($\mu_{sat}$) of TFTs were calculated using:

$$I_D = \frac{W\mu C_i}{2L}(V_G - V_{th})^2 \qquad (1)$$

where $C_i$ is the areal capacitance of the dielectric; $V_{th}$ is the threshold voltage obtained by fitting the saturation region of $I_D^{1/2}$ versus $V_G$ plots and extrapolating the fitted line to $I_D = 0$; $W$ and $L$ are the channel width and length, respectively. To avoid mobility overestimation by the edge current,[13] the channel was etched to be shorter than the S/D electrodes, as shown in Figure S2a, Supporting Information. Furthermore, to avoid other mobility overestimation pitfalls,[14] gate leakage current ($I_G$) versus $V_G$ and $I_D^{1/2}$ versus $V_G$ plots are also shown in Figure 2b,c. It could be seen that the fitted lines of $I_D^{1/2}$ versus $V_G$ plots displayed good linearity.

The pure $In_2O_3$ TFTs exhibited a $\mu_{sat}$ of as high as 51.1 cm² V⁻¹ s⁻¹, but it showed a very negative turn-on voltage ($V_{on}$, defined by the $V_{GS}$ when the $I_D$ is 10 nA) of −6.0 V. It indicated that the free carrier density of the pure $In_2O_3$ films was high. After Tb doping, the $\mu_{sat}$ decreased slightly to 45.0 cm² V⁻¹ s⁻¹, and the $V_{on}$ was closer to 0 V (−1.1 V). These results suggest that Tb doping would reduce the free carriers. The properties of the $In_2O_3$ and $Tb:In_2O_3$ TFTs are summarized in **Table 1**.

**Table 1.** Properties of the TFTs with/without Tb doping.

| Channel | $\mu_{sat}$ [cm$^2$ V$^{-1}$ s$^{-1}$]$^{-1}$ | $V_{on}/V$ | $I_{on}/I_{off}$ | $\Delta V_{on}$(NBIS)/V |
|---|---|---|---|---|
| In$_2$O$_3$ | 51.1 | −6.0 | ≈10$^8$ | −11.7 |
| Tb:In$_2$O$_3$ | 45.0 | −1.1 | ≈10$^8$ | −3.9 |

Figure 2d shows the $V_G$ dependent $\mu_{sat}$ of the Tb:In$_2$O$_3$ TFT. It could be seen that the $\mu_{sat}$ was higher than 40 cm$^2$ V$^{-1}$ s$^{-1}$ in a wide $V_G$ range (about 8–16 V), and the peak of $\mu_{sat}$ was located at about 11 V. To verify the reproducibility of the Tb:In$_2$O$_3$ TFTs, we fabricated 125 Tb:In$_2$O$_3$ (5 wt.%) TFTs with the same condition. The mobility distribution histogram of the 125 TFTs is shown in Figure 2e. All the devices exhibited mobilities between 30 and 55 cm$^2$ V$^{-1}$ s$^{-1}$, and most of them exhibited mobilities between 35 and 45 cm$^2$ V$^{-1}$ s$^{-1}$. Three devices even exhibited mobilities higher than 50 cm$^2$ V$^{-1}$ s$^{-1}$ (with the highest mobility of as high as 54.0 cm$^2$ V$^{-1}$ s$^{-1}$). Therefore, the high mobility of the Tb:In$_2$O$_3$ (5 wt.%) TFTs is reliable. We ascribe the high mobility of the Tb:In$_2$O$_3$ TFTs to the low Tb doping amount and less lattice distortion (as shown in Figure 1) which hardly destroys the spatial overlap between the vacant In5s orbitals in low doping amounts.

To investigate the NBIS stability of the Tb:In$_2$O$_3$ TFTs, the devices with In$_2$O$_3$ or Tb:In$_2$O$_3$ channel layers were tested under a negative $V_G$ stress of −20 V combined with an illumination stress of 250-Lux white LED light. As shown in **Figure 3**, after NBIS for 1 h, the pristine In$_2$O$_3$ TFTs showed a large negative $V_{on}$ shift ($\Delta V_{on}$, defined by the gate voltage shift at $I_D$ =10$^{-8}$A) of −11.7 V, while the devices with Tb:In$_2$O$_3$ channel exhibited much smaller $\Delta V_{on}$ of −3.9 V (with average $\Delta V_{on}$ of 4.0 V). To the best of our knowledge, it is the first AOS TFT with single-layer channel that has an effectively improved NBIS stability and a saturation mobility higher than 40 cm$^2$ V$^{-1}$ s$^{-1}$ without notable overestimation pitfalls. The result indicates that the tradeoff between the mobility and NBIS stability can be reduced significantly by small amount of Tb$_4$O$_7$ doping. It should be noted that the improvement of NBIS stability after Tb doping is not owing to the reducing of the V$_O$ concentration, because our previous study on solution-processed In$_2$O$_3$ TFTs doped with different lanthanides shows that there are no direct relationships between the NBIS stability and the V$_O$ concentration.[11] And recent work reported by Liang and Cao et al. also reveals that the contents of V$_O$ between InSnZnO and Pr-doped InSnZnO show few differences, but the differences in photostability are significant.[15]

To investigate the effect of Tb doping on the NBIS stability, the valance states of the Tb in the Tb:In$_2$O$_3$ should be identified. Figure S3, Supporting Information, shows the Tb 3$d$ spectra of the 5 wt.% Tb$_4$O$_7$ doping In$_2$O$_3$ film. The parameters of the fitting peaks are summarized in Table S1, Supporting Information.[16] The ratio of Tb$_2$O$_3$ to TbO$_2$ were calculated by the peak area to be 49.8%:50.2%, very close to that in Tb$_4$O$_7$ (1:1).

To verify the CT transition of Tb$^{4+}$ taking place during light illumination, UV-visible absorption and reflection spectra were measured. Because the In$_2$O$_3$ and Tb:In$_2$O$_3$ thin films were highly transparent in the visible range and the Tb content was low, there was no clear difference in the absorption spectra between the In$_2$O$_3$ and Tb:In$_2$O$_3$ thin films. Therefore, the reflection spectra of the In$_2$O$_3$ and Tb:In$_2$O$_3$ targets instead of thin films were measured. **Figure 4** shows the reflection spectra of the In$_2$O$_3$ and Tb:In$_2$O$_3$ targets. The reflection of the pure In$_2$O$_3$ target between 450 and 830 nm was high (≈90%), revealing low absorption (because all the targets were untransparent). In contrast, the reflection of the Tb:In$_2$O$_3$ target in the same range (450–830 nm) was low (≈20%), indicating high absorption. The broad absorption in the visible range of the Tb:In$_2$O$_3$ target is most likely to be due to the CT transition of the Tb$^{4+}$, which has strong and broad absorption in the visible range.[17–19] We ascribe the improvement of NBIS stability of the Tb:In$_2$O$_3$ to the CT transition of Tb$^{4+}$ as discussed below.

It is known that high-density subgap states are formed by V$_O$ existed in AOSs near valance band maximum (VBM). Under light illumination, some of the V$_O$ will be thermal excited and lose two electrons and become Vo$^{2+}$ (see **Figure 5**). The transition of the V$_O$ ground state to Vo$^{2+}$ excited states causes spontaneous outward relaxation, which makes the Vo$^{2+}$ level act as a sub-gap state below the conduction band minimum (CBM), contributing the delocalized free electrons in the conduction band.[3–8] The relaxation for V$_O$ to Vo$^{2+}$ is strong, because of the electrostatic repulsion of the two positive charges in Vo$^{2+}$ (e.g., the V$_O$ of ZnO causes 12% inward relaxation, and Vo$^{2+}$ causes 24% outward relaxation).[3] The strong relaxation causes large lattice expansion/contraction during V$_O$ ionization/recombination. As a result, V$_O$ ionization/ recombination process is very slow, leading to a very long decade time of the photocurrent (>10$^4$ s).[20,21]

When the AOSs are doped with Tb, CT transition takes place during light illumination. Figure 5 illustrates the CT transition process and the band alignment of the LnO$_2$ and In$_2$O$_3$. Initially, the system is at Point A on Parabola (4$f^n$) corresponding with an electron at the top of the valence band and a Tb$^{4+}$ ion (Tb4$f^7$—O2$p^6$). Under light illumination, the initial state transfers to Point B of the Tb$^{3+}$ state (Tb4$f^8$—O2$p^5$). Because Tb$^{3+}$ has ≈0.16 Å larger ionic radius than Tb$^{4+}$, it relaxes outward and moves to Point C. At the same time, O2$p^5$ has a smaller radius than O2$p^6$, resulting in inward relaxation. Therefore, the overall lattice expansion/contraction from Tb4$f^7$—O2$p^6$ state to Tb4$f^8$—O2$p^5$ state is relatively small. Moreover, the Coulomb attraction between the hole (O2$p^5$) and the transferred electron reduces the relaxation time.[22] Therefore, compared to V$_O$ ionization process, the CT transition process has a much shorter relaxation time. As a result, Tb$^{4+}$ is more easily to absorb light than V$_O$. It means that the incident light is more
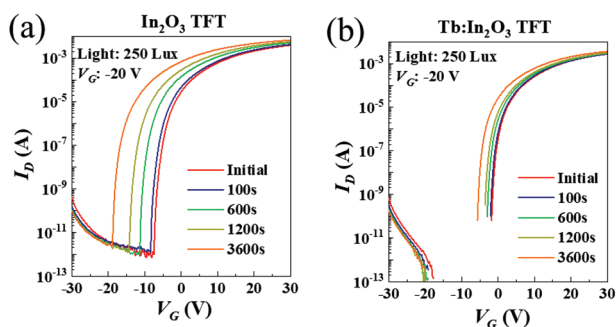


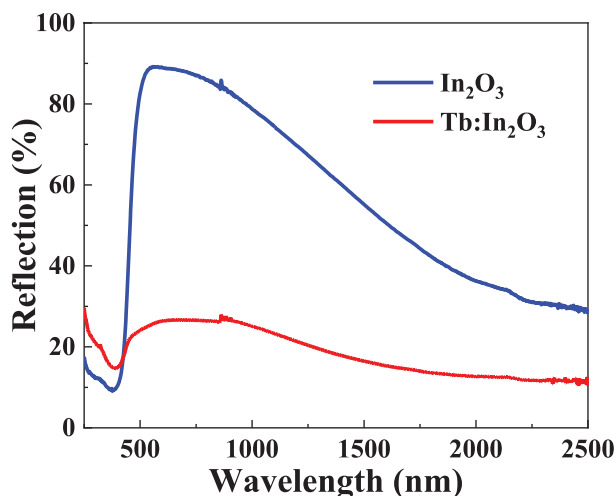**Figure 3.** Transfer curves evolution of a) In$_2$O$_3$ and b) Tb:In$_2$O$_3$ TFTs under 3600s NBIS.

**ADVANCED
SCIENCE NEWS**

www.advancedsciencenews.com

**ADVANCED
ELECTRONIC
MATERIALS**

www.advelectronicmat.de

**Figure 4.** Reflection spectra of the $In_2O_3$ and $Tb:In_2O_3$ targets.



**Figure 6.** The $\mu$-PCD decade curves of the $In_2O_3$, $Tb:In_2O_3$, and $La:In_2O_3$ films.

easily to be absorbed by $Tb^{4+}(Tb4f^7-O2p^6)$, which transfers to $Tb4f^8-O2p^5$ state. Then, it transfers back to Parabola ($4f^7$) by crossing relaxation where all luminescence is quenched,[22–24] which is proved by the photoluminescence (PL) spectroscopy (no luminescence related to Tb was found, see Figure S4, Supporting Information). The PL spectroscopy also implies that the $Tb4f^8$ will not relax to the excited state of $Tb4f^7$ and causing $f$-$f$ emission from excited state to the ground state of $Tb4f^7$. It may be attributed to the relatively stable half-filled (7 $f$ electrons) $f$ orbital of $Tb4f^7$. The results reveal that the CT transition absorbs the incident light and downconverts it to nonradiative transition with a relatively short relaxation time.

Next, the intersystem relaxation between Tb and $V_O$ was considered and discussed. As discussed above, a small part of the blue light is inevitably absorbed by $V_O$, which is then ionized to $V_O^{2+}$, contributing two delocalized free electrons to the conduction band. Since the electrons released by $V_O$ is delocalized, they may be trapped by the holes in the $Tb4f^8-O2p^5$ states which are closed to the CBM of $In_2O_3$ (see Figure 5), leading to outward relaxation and facilitating the crossing relaxation ($4f^8 \rightarrow 4f^7$). At the same time, the outward relaxation may help the $V_O^{2+}$ relaxing back to $V_O$.
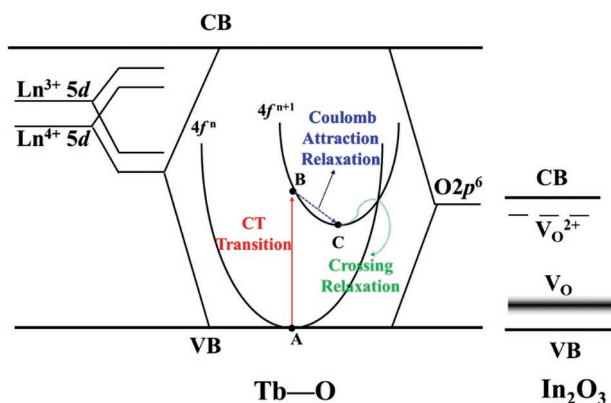


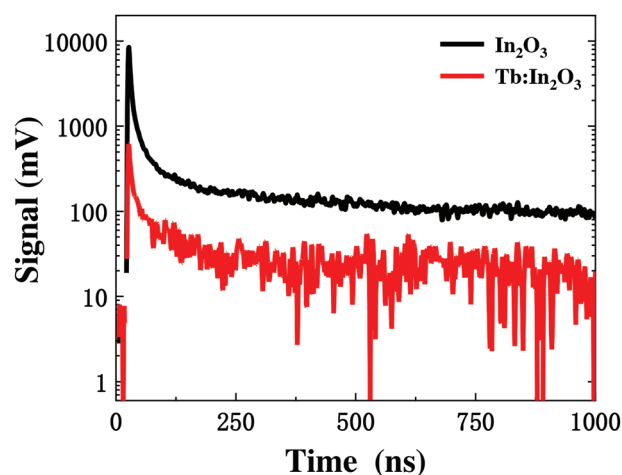**Figure 5.** Illustration of the CT transition process and the band alignment of the $LnO_2$ and $In_2O_3$.

To measure the lifetime of the photo-induced electrons, microwave photoconductivity decay ($\mu$-PCD) experiments were performed. **Figure 6** shows the decade curves of the different films (the corresponding peak level mappings are shown in Figure S5, Supporting Information). Since the number of photo-induced electrons is much larger than that of the intrinsic free electrons under dark condition, the peak level of $\mu$-PCD is mainly contributed from photo-induced electrons. It can be seen from Figure S5, Supporting Information that the peak level of $In_2O_3$ is nearly one order higher than that of $Tb:In_2O_3$, which indicates that $In_2O_3$ is much more sensitive to the incident light than $Tb:In_2O_3$. It is worth noting that the number of the photo-induced electrons is irrelevant to the number of intrinsic free electrons or $V_O$, because most of the other lanthanide-doped $In_2O_3$ semiconductors (such as $La:In_2O_3$ which has low $V_O$ density but poor NBIS stability)[25] also have large peak level. To evaluate the lifetime of the photo-induced electrons, the decade curves were fitted by the following equation,[26]

$$n(t) = n_0 \left( \exp\left(-\frac{t}{\tau_1}\right) + \exp\left(-\left(\frac{t}{\tau_2}\right)^\beta\right) \right) \quad (2)$$

where $n_0$ is the 1/2 of the carrier density immediately after photoexcitation (at $t = 0$); $\tau_1$ is the fast decay constant that may represent the direct electron-hole recombination or the deep-level recombination centers such as the Vo and the Tb-related traps; $\tau_2$ is the slow decay constant that is the result of trapped carriers being reemitted into the conduction band, followed immediately by the occurrence of eventual recombination process or reemitted carriers again being trapped; and $\beta$ is the stretching exponent.[27] The fitted curves are shown in Figure S6, Supporting Information, and the corresponding fitted parameters are summarized in **Table 2**. Although $Tb:In_2O_3$ has a much lower photo-induced electron density ($2n_0$), it has a shorter $\tau_1$ than $In_2O_3$. It implies that the $Tb4f^8-O2p^5$ states may act as the recombination centers that help the photo-induced electrons recombine. In contrary to the $\tau_1$, the $\tau_2$ of $Tb:In_2O_3$ is slightly longer than that of $In_2O_3$, which means that a small number of shallow defects may form after $Tb^{4+}$ doping. However, the

**Table 2.** Summary of stretched exponential analysis of the fitted $\mu$-PCD decade curves.

| Films | $n_0$ [mV]$^{-1}$ | $\tau_1$ [ns]$^{-1}$ | $\tau_2$ [ns]$^{-1}$ | $\beta$ |
|---|---|---|---|---|
| $In_2O_3$ | 4857 | 11.22 | 10.85 | 0.31 |
| $Tb:In_2O_3$ | 569 | 7.23 | 13.30 | 0.28 |

changes in both $\tau_1$ and $\tau_2$ after $Tb^{4+}$ doping are too small to fully explain the significant improvement of the NBIS stability. In fact, the NBIS stability is more strongly related to the number of photo-induced electrons ($2n_0$).

As discussed above, the CT transition of $Tb^{4+}$ absorbs most of the incident blue light due to the smaller lattice expansion/contraction and shorter relaxation time compared to $V_O$ ionization, but the electron in CT transition just transfers from ligand ($O2p$) to tetravalent ion ($Tb4f$) and it will not be exited to the conduction band by the light, because the conduction band of the $TbO_2$ formed by the antibonding state of $Tb5d$—$O2p$ is far above from the $Tb4f^8$—$O2p^5$ states (see Figure 5).[22,28] Therefore, most of the the transferred electrons during the CT transition process are localized. This is the reason why $Tb:In_2O_3$ absorbs much more light than $In_2O_3$ (Figure 4) while it has much fewer light-induced electrons (Figure S5, Supporting Information). It means that the CT transition in $Tb:In_2O_3$ is mainly in a self-circulation process with only a little interaction with $V_O$. The above analysis reveals that the effective improvement of NBIS stability after $Tb^{4+}$ doping is mainly attributed to the absorption of the incident blue light by the $Tb4f^7$—$O2p^6$ to $Tb4f^8$—$O2p^5$ CT transition that has a smaller overall lattice expansion/contraction and shorter relaxation time compared to $V_O$ ionization. Most of the $Tb4f^8$—$O2p^5$ excited states downconvert to nonradiative transition by cross relaxation, and some of them may act as the recombination centers that help the photo-induced electrons recombine.

## 3. Conclusion

In conclusion, a tetravalent-terbium-doped indium oxide ($Tb:In_2O_3$) AOS was introduced to effectively improve the NBIS stability of the TFT while ensuring high mobility. The TFT with $Tb:In_2O_3$ channel layer exhibited remarkable characteristics with a $\mu_{sat}$ of 45.0 cm$^2$ V$^{-1}$ s$^{-1}$ and a $\Delta V_{on}$ of −3.9 V under 3600 s NBIS (compared to a $\mu_{sat}$ of 51.1 cm$^2$ V$^{-1}$ s$^{-1}$ and a $\Delta V_{on}$ of −11.7 V for pure $In_2O_3$ TFTs without Tb doping), indicating that the tradeoff between the mobility and NBIS stability can be reduced significantly by $Tb^{4+}$ doping. To the best of our knowledge, it is the first AOS TFT with a single-layer channel that has an effectively improved NBIS stability and a saturation mobility higher than 40 cm$^2$ V$^{-1}$ s$^{-1}$ without notable overestimation pitfalls. Comprehensive studies reveal that the effective improvement of NBIS stability after $Tb^{4+}$ doping is mainly attributed to the absorption of the incident blue light by the $Tb4f^7$—$O2p^6$ to $Tb4f^8$—$O2p^5$ CT transition that has smaller overall lattice expansion/contraction and shorter relaxation time compared to $V_O$ ionization. And most of the $Tb4f^8$—$O2p^5$ excited states downconvert to nonradiative transition by cross relaxation, and some of them may act

as the recombination centers that help the photo-induced electrons recombine.

## 4. Experimental Section

Bottom-gate structure was employed to fabricate the AOS TFTs. First, a 300 nm thick aluminum-neodymium alloy (Al:Nd) gate layer was prepared on the glass substrate by sputtering. Then, the surface of Al:Nd layer was anodized, forming a 140-nm-thick layer of AlOx:Nd.[29] The channel layer (12 nm) was deposited from $Tb:In_2O_3$ target ($Tb_4O_7:In_2O_3$ = 5:95 wt.%, the raw material is $Tb_4O_7$, containing $Tb^{3+}$ and $Tb^{4+}$) by magnetron sputtering at room temperature in $Ar/O_2$ (3.6/4 SCCM) atmosphere and patterned by a shadow mask (see Figure S2a, Supporting Information). Next, the channel layer was annealed at 400 °C for 1 h in air atmosphere. After that, a 200/100 nm thick Mo/Al was deposited by dc sputtering and patterned by a shadow mask to form source and drain electrodes. The channel length ($L$) and width ($W$) were 200 μm and 800 μm, respectively. Finally, the whole devices were annealed at 150 °C for 1 h in air atmosphere. For comparison, TFTs with pure $In_2O_3$ channel (12 nm) were fabricated in the same condition as mentioned above.

The electrical characteristics of $In_2O_3$ and $Tb:In_2O_3$ TFTs were measured by a semiconductor parameter analyzer (Keysight B1500). The crystallization characteristics of films (300 nm, annealed at 400 °C for 1 h) were determined by XRD (Rigaku Smartlab; scanning mode: 2Theta; scanning type: continuous scanning; voltage/current: 40 kv/100 mA; step: 0.02°; speed: 10° min$^{-1}$). The reflection spectrum was measured by PE-Lambda950. The lifetime of the photo-induced electrons was measured by $\mu$-PCD (KOBELCO, LTA-1620 SP, Kobe, Japan).

## Supporting Information

Supporting Information is available from the Wiley Online Library or from the author.

## Conflict of Interest

The authors declare no conflict of interest.

## Data Availability Statement

Research data are not shared.

**ADVANCED
SCIENCE NEWS**

www.advancedsciencenews.com

**ADVANCED
ELECTRONIC
MATERIALS**

www.advelectronicmat.de

[1] K. Nomura, H. Ohta, A. Takagi, T. Kamiya, M. Hirano, H. Hosono, *Nature* **2004**, *432*, 488.

[2] T.-K. Chang, C.-W. Lin, S. Chang, *SID Symp. Dig. Tech. Pap.* **2019**, *50*, 545.

[3] A. Janotti, C. G. V. D. Walle, *Appl. Phys. Lett.* **2005**, *87*, 122102.

[4] S. Lany, A. Zunger, *Phys. Rev. B* **2005**, *72*, 035215.

[5] A. Janotti, C. G. Van de Walle, *Phys. Rev. B* **2007**, *76*, 165202.

[6] J. K. Jeong, *J. Mater. Res.* **2013**, *28*, 2071.

[7] A. J. Flewitt, M. J. Powell, *J. Appl. Phys.* **2014**, *115*, 134501.

[8] T. Long, X. Dai, L. Lan, C. Deng, Z. Chen, C. He, L. Liu, X. Yang, J. Peng, *J. Mater. Chem. C* **2019**, *7*, 13960.

[9] J. Kim, J. Bang, N. Nakamura, H. Hosono, *APL Mater.* **2019**, *7*, 022501.

[10] Y.-S. Shiah, K. Sim, Y. Shi, K. Abe, S. Ueda, M. Sasase, J. Kim, H. Hosono, *Nat. Electron.* **2021**, *4*, 800.

[11] P. He, H. Xu, L. Lan, C. Deng, Y. Wu, Y. Lin, S. Chen, C. Ding, X. Li, M. Xu, J. Peng, *Commun. Mater.* **2021**, *2*, 86.

[12] I. Hamberg, C. G. Granqvist, *J. Appl. Phys.* **1986**, *60*, R123.

[13] C. Chen, Z. Chen, K. Xu, J. Zheng, H. Ou, Z. Wang, H. Chen, X. Liu, Q. Wu, P. K. L. Chan, C. Liu, *IEEE Electron Devices Lett.* **2019**, *40*, 897.

[14] H. H. Choi, K. Cho, C. D. Frisbie, H. Sirringhaus, V. Podzorov, *Nat. Mater.* **2017**, *17*, 2.

[15] H. Zhang, L. Liang, X. Wang, Z. Wu, H. Cao, *IEEE Trans. Electron Devices* **2022**, *69*, 152.

[16] S. Gu, W. Li, Y. Bian, F. Wang, H. Li, X. Liu, *J. Phys. Chem. C* **2016**, *120*, 19242.

[17] D. E. Hobart, K. Samhoun, J. P. Young, V. E. Norvell, G. Mamantov, J. R. Peterson, *Inorg. Nucl. Chem. Lett.* **1980**, *16*, 321.

[18] G. Blasse, *Prog. Solid State Chem.* **1988**, *18*, 79.

[19] T. Gorai, W. Schmitt, T. Gunnlaugsson, *Dalton Trans.* **2021**, *50*, 770.

[20] D. H. Lee, K.-I. Kawamura, K. Nomura, T. Kamiya, H. Hosono, *Electrochem. Solid-State Lett.* **2010**, *13*, H324.

[21] S. Mondal, A. K. Raychaudhuri, *Appl. Phys. Lett.* **2011**, *98*, 023501.

[22] P. Dorenbos, *J. Phys.: Condens. Matter* **2003**, *15*, 8417.

[23] J. Hölsä, T. Aitasalo, H. Jungner, M. Lastusaari, J. Niittykoski, G. Spano, *J. Alloys Compd.* **2004**, *374*, 56.

[24] E. Zych, P. J. Dereń, W. Strek, A. Meijerink, W. Mielcarek, K. Domagala, *J. Alloys Compd.* **2001**, *323–324*, 8.

[25] Z. Lin, L. Lan, P. Xiao, S. Sun, Y. Li, W. Song, P. Gao, E. Song, P. Zhang, L. Wang, H. Ning, J. Peng, *IEEE Electron Device Lett.* **2016**, *37*, 1139.

[26] S. Yasuno, T. Kita, S. Morita, T. Kugimiya, K. Hayashi, S. Sumie, *J. Appl. Phys.* **2012**, *112*, 053715.

[27] H. X. Jiang, J. Y. Lin, *Phys. Rev. Lett.* **1990**, *64*, 2547.

[28] L. Petit, A. Svane, Z. Szotek, W. M. Temmerman, *Phys. Rev. B* **2005**, *72*, 205118.

[29] L. Lan, M. Zhao, N. Xiong, P. Xiao, W. Shi, M. Xu, J. Peng, *IEEE Electron Device Lett.* **2012**, *33*, 827.

**2200187 (6 of 6)**